Available on the CERN CDS information server **CMS PAS HIG-16-037**

CMS Physics Analysis Summary

Contact: cms-pag-conveners-higgs@cern.ch 2016/11/09

Search for a neutral MSSM Higgs boson decaying into $\tau\tau$ with 12.9 fb^{-1} of data at $\sqrt{s} = 13$ TeV

The CMS Collaboration

Abstract

A search for a neutral Higgs boson is presented, using the decay into two tau leptons. The analysis uses 12.9 fb^{-1} of pp collision data collected by CMS in 2016, at a centre of mass energy of 13 TeV. The results are interpreted in the context of the minimal supersymmetric standard model. No excess above the expectation from the standard model is found and upper limits are set on the production cross sections times branching fraction for masses between 90 and 3200 GeV. Regions of phase space of two different benchmark scenarios are also excluded.

1 Introduction

The discovery of a scalar boson by the ATLAS and CMS experiments in 2012 [1, 2] led to a new era in physics. Since then increasing numbers of experimental measurements have shown consistency with the standard model (SM) [3–8] with a Higgs boson at a mass of 125.09 ± 0.21(stat.)± 0.11(syst.) GeV [9–12]. However, the SM is known not to be complete, and a number of favoured beyond the standard model (BSM) theories include an extended Higgs sector [13, 14]. As such, study of any potential deviations from the SM predictions in the properties of the existing Higgs boson, together with searches for possible additional Higgs bosons, are essential in the hunt for new physics.

There exist many possible extensions of the SM, and one of the simplest is the minimal supersymmetric standard model (MSSM), which incorporates supersymmetry. This invokes a symmetry between bosons and fermions, introducing additional heavier partners for the existing particles, and allowing for possible cancellation of the quadratically divergent self-energy corrections to the Higgs mass at high energy [15, 16].

The Higgs sector of the MSSM consists of two Higgs doublets, one of which couples to up-type fermions and one to down-type fermions. This leads to five physical Higgs particles: two charged Higgs bosons $\mathrm{H}^{\pm}$, two neutral scalar Higgs bosons h and H and one neutral pseudoscalar A. It is conventional to make use of the notation ϕ to represent any one of the three neutral Higgs bosons, $\phi = \mathrm{h}, \mathrm{H}, \mathrm{A}$.

The MSSM is expressed in terms of two free parameters at tree level, usually chosen to be the mass of the pseudoscalar Higgs boson, m_{A}, and the ratio of vacuum expectation values of the two doublets, $\tan\beta$. For a large number of MSSM models which have small and medium values of $\tan\beta$, the dominant production mode is gluon fusion as in the SM. The existence of the second Higgs doublet means that for large values of $\tan\beta$ couplings to down-type fermions are enhanced. This leads to two effects: enhanced rate of decays into taus, and a second dominant production mode, b associated production. The leading order diagrams for the gluon fusion production process and the b associated production process in the four and five–flavour scheme can be seen in Figure 1.

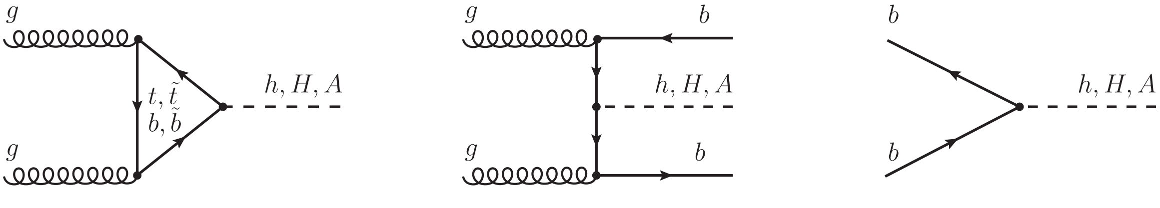

(a) (b) (c)

Figure 1: Leading order diagrams of the a) gluon fusion and b) four-flavour and c) five-flavour schemes for b associated production of the Higgs boson in the MSSM.

Radiative corrections lead to large modifications of the behaviour beyond tree level. These can depend on a large number of different supersymmetry parameters. For simplicity these parameters are typically fixed to sensible choices based on experimental results and theoretical arguments. Each choice results in a different so-called “benchmark” scenario. These choices must produce MSSM models which are consistent with the discovered 125 GeV Higgs boson. The scenarios considered in this report are the $m_{\mathrm{h}}^{\mathrm{mod}+}$ and hMSSM scenarios [17, 18]. Both scenarios have been used previously in results from the ATLAS and CMS collaborations. In the case of the $m_{\mathrm{h}}^{\mathrm{mod+}}$ scenario, choices are made for the supersymmetry parameters which allow the majority of the $m_{\mathrm{A}} - tan\beta$ plane to be consistent with a scalar Higgs boson with a mass of 125 GeV. In the case of the hMSSM scenario, the condition of $m_{\mathrm{h}} = 125\,\mathrm{GeV}$ is fixed across the whole plane and the radiative corrections adjusted accordingly.

Previous searches have not found any evidence for the MSSM, although a large amount of the possible phase space remains non-excluded. Constraints are placed by previous direct searches for MSSM Higgs bosons decaying into a pair of tau leptons from Run 1 of the LHC [19–21]. The first of such searches in Run 2 making use of the dataset from 2015, already exceeded the sensitivity of the Run 1 dataset at higher masses [22, 23], whilst the increasing dataset from 2016 running allows us to probe previously unreached phase space. Results already released by ATLAS still show no evidence for MSSM after adding the first part of the 2016 data [24].

In this report, the first results of direct searches for MSSM Higgs bosons decaying into a pair of tau leptons from the CMS collaboration using the data from 2016 running are presented. The dataset amounts to an integrated luminosity of $12.9\,\mathrm{fb}^{-1}$ all taken during the 2016 running period at a centre of mass energy of 13 TeV. The analysis is performed in four different final states of the taus: $\mathrm{e}\mu$, $\mathrm{e}\tau_{\mathrm{h}}$, $\mu\tau_{\mathrm{h}}$ and $\tau_{\mathrm{h}}\tau_{\mathrm{h}}$, where τ_{h} indicates a tau decaying hadronically.

2 The CMS detector

The central feature of the CMS apparatus is a superconducting solenoid of 6 m internal diameter providing a field of 3.8 T. Within the field volume are a silicon pixel and strip tracker, a crystal electromagnetic calorimeter (ECAL), and a brass/scintillator hadron calorimeter (HCAL), each composed of a barrel and two endcap sections. Muons are measured in gas-ionisation detectors embedded in the steel return yoke of the magnet. The first level (L1) of the CMS trigger system, composed of custom hardware processors, uses information from the calorimeters and muon detectors to select the most interesting events in a fixed time interval of less than $4\,\mu$s. The high-level Trigger processor farm decreases the L1 accept rate from around 100 kHz to approximately 1.2 kHz before data storage (a further 0.6 kHz of data is “parked” to be reconstructed and analyzed at a later date).

A more detailed description of the CMS detector together with a description of the coordinate system and main kinematic variables used in the analysis can be found in [25].

3 Event reconstruction

The reconstruction of the event is based on a particle-flow (PF) algorithm [26, 27], which combines information from all CMS subdetectors to reconstruct individual particle candidates: muons, electrons, photons, charged and neutral hadrons. Jets, hadronically decaying τ leptons and missing transverse energy are then constructed using the inputs of the individual particles candidates.

The deterministic annealing algorithm is used to reconstruct collision vertices [28]. The primary vertex of the hard interaction is assigned as the vertex with the maximum sum of squared transverse momenta calculated from all associated tracks. Muons, electrons, and hadronically decaying τ leptons are required to originate from the primary vertex of the hard interaction. All other vertices are considered to come from additional inelastic proton-proton collisions in each bunch crossing, referred to as “pileup”.

Electrons are reconstructed by combining clusters of ECAL energy deposits with hits in the silicon tracker [29]. Electrons are also required to pass an identification (ID) requirement based on a Boosted Decision Tree (BDT) discriminator with inputs based on information on track quality, shower shape and kinematic quantities [30]. Different working points exist corresponding to different signal efficiencies; in this analysis the working points with 80% and 90% signal efficiency are used. Muons are reconstructed by performing simultaneously a global track fit to hits in the silicon tracker and in the muon system [31]. Different working points are defined based on stronger or looser requirements on the quality of these fits; in this analysis an ID working point which is referred to as "medium" is used which has a signal efficiency of around 99%.

The contribution from backgrounds is reduced by placing conditions on the isolation of the electron or muon. Relative isolation I_{ℓ}^{rel} (where ℓ denotes an electron or muon) is measured relative to the candidate's transverse momentum. It is computed by summing the charged and neutral particles reconstructed by the PF algorithm in a cone of radius $\Delta\mathrm{R} = \sqrt{(\Delta\eta^2) + (\Delta\phi^2)} < 0.3(0.4)$ around the lepton direction at the interaction vertex for electrons (muons), where $\Delta\eta$ and $\Delta\phi$ quantify the angular distance of the PF candidate from the lepton in the η and ϕ directions. The presence of neutral particles from pileup vertices is accounted for by summing the transverse momenta of charged hadrons from pileup vertices in the isolation cone, and multiplying by a factor of 0.5 to account for the approximate ratio of neutral to charged hadron production. This is then subtracted from the computed isolation. Finally the computed isolation is divided by the transverse momentum of the lepton to yield I_{ℓ}^{rel}.

Jets are reconstructed from PF candidates using the anti-k_t jet clustering algorithm implemented in FASTJET [32, 33] with a distance parameter of 0.4. Jets resulting from the hadronization of b quarks (b jets) are identified using the combined secondary vertex (CSV) b tagging algorithm [34], which exploits the information on the decay vertices of long-lived mesons and the impact parameters of charged particle tracks, combined in a likelihood discriminant. Working points are defined based on the mistag rate; the working point corresponding to a mistag rate of 1% and a b tagging efficiency rate of approximately 70% is referred to as "medium" and is used in this analysis.

Hadronically decaying τ leptons are reconstructed using the hadron-plus-dynamic-strips algorithm [35]. The algorithm is seeded by a PF jet and considers candidates with one charged pion and up to two neutral pions, or three charged pions. The neutral pions decay rapidly into two photons, and are reconstructed as "strips" of electromagnetic particles, formed with dynamic size from energy depositions in the ECAL. The tau decay mode is reconstructed by combining the charged hadrons with the ECAL strips. The τ_{h} candidates that are also compatible with muons or electrons are rejected. The contribution from jets originating from the hadronization of quarks and gluons being reconstructed as taus is suppressed by requiring the τ_{h} candidate to be isolated. The isolation variable is computed using a multivariate (MVA) approach [36], combining ID and isolation variables with lifetime information. This has significantly improved fake τ_{h} rejection compared with the cut-based isolation used for the electrons and muons. Different working points for the MVA tau isolation are defined which correspond to particular choices for signal efficiency and fake rates, the optimal choice depending on the expected contributions of real and fake taus in a given event selection. In this analysis working points all the way from "loose" to "tight" are used in the various signal and sideband regions. Finally requirements are applied on additional multivariate discriminants which reduce contributions from electrons or muons which are reconstructed as taus. These are generally referred to as anti-electron or anti-muon discriminators and also exist in different working points in the range "very loose" to "tight".

The missing transverse momentum vector $\vec{p}_{\mathrm{T}}^{\mathrm{miss}}$ is defined as the negative vector sum of the transverse momenta of all reconstructed PF particles. Its magnitude is referred to as $E_{\mathrm{T}}^{\mathrm{miss}}$. In order to mitigate the effects of pileup, a multivariate regression correction of $E_{\mathrm{T}}^{\mathrm{miss}}$ is used where the contributing particles are separated into those coming from the primary vertex and those that are not [37]. The correction is found to improve the $E_{\mathrm{T}}^{\mathrm{miss}}$ resolution in $\mathrm{Z} \to \mu\mu$ events.

The two types of MSSM signal and many of the backgrounds are simulated using Monte Carlo (MC) simulation. Samples of gluon fusion and b associated production signal events were generated using PYTHIA 8 [38], for a range of signal masses between $m_{\Phi} = 90$ GeV and $m_{\Phi} = 3200$ GeV. For the Drell-Yan $\mathrm{Z}/\gamma^{*} \to \tau\tau$ and W+jets backgrounds, samples were generated with MADGRAPH 5. Additional samples have been generated with different numbers of outgoing partons in the hard interaction and combined in order to increase statistics in regions of high signal purity. For the $\mathrm{t\bar{t}}$ and single top processes samples were generated with POWHEG [39, 40], while for diboson processes (WW, WZ and ZZ) MADGRAPH 5_AMC@NLO was used [39]. For the model dependent results the SM Higgs boson prediction is used, and this is simulated using POWHEG [39, 40] separately for the gluon fusion, vector boson fusion (VBF) and associated production in association with a Z boson (ZH) and W boson (WH). For all samples, hadronic shower and hadronization processes are modelled using PYTHIA 8. All simulated samples are also corrected for the observed distribution of pileup. In the 2016 data taking period included in these results the average number of pileup collisions per event was 24.

4 Event selection and categorization

The analysis is performed in the four most sensitive final states of the di-tau pair: $\mathrm{e}\mu$, $\mathrm{e}\tau_{\mathrm{h}}$, $\mu\tau_{\mathrm{h}}$, and $\tau_{\mathrm{h}}\tau_{\mathrm{h}}$, which are generally referred to as "channels". The selections and triggers used are to a large extent channel-dependent. For the $\mathrm{e}\tau_{\mathrm{h}}$ and $\mu\tau_{\mathrm{h}}$ channels, triggers are based on at least one electron or muon object. For the $\mathrm{e}\mu$ channel, lower threshold triggers are used which require the presence of both an electron and muon; an "or" of two such triggers is used in which there is one lower p_{T} object and one higher p_{T} object. In the $\tau_{\mathrm{h}}\tau_{\mathrm{h}}$ channel, a trigger based on two hadronic taus is used. On top of the trigger selection additional p_{T} and η cuts are applied - the minimal requirement is to retain events above the threshold of the trigger and within geometric acceptance, but also cuts can be tightened further in order to increase sensitivity to signal over background. In the $\mathrm{e}\tau_{\mathrm{h}}$ ($\mu\tau_{\mathrm{h}}$) channel, a hadronic tau is required with $p_{\mathrm{T}} >30$ GeV and $|\eta| < 2.3$ in addition to an electron (muon) with $p_{\mathrm{T}} >26$ GeV and $|\eta| < 2.1$ ($p_{\mathrm{T}} >23$ GeV and $|\eta| < 2.1$). In the $\mathrm{e}\mu$ channel, an electron with $p_{\mathrm{T}} >13$ GeV and $|\eta| < 2.5$ and a muon with $p_{\mathrm{T}} >10$ GeV and $|\eta| < 2.4$ are required, with an additional p_{T} cut of $p_{\mathrm{T}} > 24$ GeV applied to the higher p_{T} object in the case that only one of the two triggers is fired. In the $\tau_{\mathrm{h}}\tau_{\mathrm{h}}$ channel, two taus are required with $p_{\mathrm{T}} >40$ GeV and $|\eta| < 2.1$.

Additional ID and isolation conditions significantly reduce the contribution from backgrounds. A signal electron is required to pass the 80% signal efficiency working point of the electron ID MVA, while a signal muon passes the "medium" ID working point, as defined in section 3. Requirements are placed on the impact parameter, or the distance in the transverse (d_{xy}) or longitudinal (d_z) directions between the leading track for a given candidate and the primary vertex. For the electron and muon candidates in the $\mathrm{e}\tau_{\mathrm{h}}$, $\mu\tau_{\mathrm{h}}$ and $\mathrm{e}\mu$ channels, the requirements are $d_{xy}^{\mu/\mathrm{e}} < 0.045$ cm and $d_{z}^{\mu/\mathrm{e}} < 0.2$ cm. For the hadronic taus, a requirement of $d_{z}^{\tau_h} < 0.2$ cm is placed using the charged constituent with the highest p_{T} track. For the isolation and anti-electron and anti-muon discriminators of the hadronic taus, different working points are available corresponding to lower or higher values of signal efficiency (and correspondingly higher or lower amounts of rejection of background from fake taus), named from "very loose" up to "very tight". In the $\tau_h\tau_h$ channel, the optimal isolation working point for signal selection over background is found to be the "tight" working point. In the $e\tau_h$ and $\mu\tau_h$ channels, the "medium" isolation working point is used. In the $\mu\tau_h$ and $\tau_h\tau_h$ channel the "very loose" working point is used for the anti-electron discriminator, whereas the "tight" working point is used in the $e\tau_h$ channel. For the anti-muon discriminator the "loose" working point is used in the $e\tau_h$ and $\tau_h\tau_h$ channels and the "tight" working point in the $\mu\tau_h$ channel. For the electron and muons conditions are placed on the relative isolation I_ℓ^{rel} corresponding to $I_e^{rel} < 0.1$ ($I_\mu^{rel} < 0.15$) in the $e\tau_h$ ($\mu\tau_h$) channel and $I_e^{rel} < 0.15$ ($I_\mu^{rel} < 0.2$) for the electron (muon) in the $e\mu$ channel.

The selected candidate pair in each channel is required to be of opposite charge and well separated in ΔR, using the condition $\Delta R > 0.5$ in the $e\tau_h$, $\mu\tau_h$ and $\tau_h\tau_h$ channels and $\Delta R > 0.3$ in $e\mu$. Backgrounds from $Z \to \ell\ell$ and diboson events are further suppressed by vetoing events with additional electrons and muons. In the $\mu\tau_h$ channel, a veto muon is defined as a muon which is reconstructed as a PF muon with hits in both the global muon system and the tracker, passing a looser isolation cut of $I_\mu^{rel} < 0.3$ and with $p_T > 15$ GeV, $|\eta| < 2.4$ and impact parameter cuts the same as for the signal muons. Similarly in the $e\tau_h$ channel a veto electron passes a cut-based electron ID which is looser than the MVA ID used for the signal electrons, a looser isolation cut of $I_e^{rel} < 0.3$ and with $p_T > 15$ GeV, $|\eta| < 2.5$ and impact parameter cuts the same as for the signal electrons. If two such veto muons (electrons) exist in a $\mu\tau_h$ ($e\tau_h$) event which have opposite sign and $\Delta R > 0.15$ then the event is vetoed. Finally a further requirement on the total number of reconstructed electrons and muons in the event is applied to remove overlap between channels. In this overlap filter a muon is defined as $p_T > 10$ GeV, $|\eta| < 2.4$ passing the "medium" muon ID, with isolation $I_\mu^{rel} < 0.3$ and impact parameter cuts the same as the signal muons and an electron is defined as $p_T > 10$ GeV, $|\eta| < 2.5$ and passing the MVA working point with 90% signal efficiency, with isolation $I_e^{rel} < 0.3$ and impact parameter cuts the same as the signal electrons. The final requirement is that there exists exactly one such muon (electron) in the $\mu\tau_h$ ($e\tau_h$) channels, zero muons (electrons) in the $e\tau_h$ ($\mu\tau_h$) channel, one electron and one muon in the $e\mu$ channel and exactly zero of each in the $\tau_h\tau_h$ channel. These preselection cuts are summarized in table 1.

Additional kinematic cuts are included to reduce the contribution of certain backgrounds. In the $e\tau_h$ and $\mu\tau_h$ channels, the transverse mass between the light lepton and the missing energy is used. This is defined as:

$$m_T = \sqrt{2 p_T E_T^{miss} (1 - \cos\Delta\phi)}, \tag{1}$$

where p_T is the lepton transverse momentum and $\Delta\phi$ is the difference in the azimuthal angle between the lepton momentum and $\vec{p}_T^{miss}$. Figure 2 shows the distribution of this variable in the $\mu\tau_h$ channel. The applied cuts for the signal region are $m_T < 50$ GeV in $e\tau_h$ and $m_T < 40$ GeV in $\mu\tau_h$, which were optimized alongside the tau isolation working point and tau p_T cut. These cuts greatly reduce the W+jets background, a control sample of which can be found using the high m_T region, as will be discussed in section 5.

In the $e\mu$ channel, the $t\bar{t}$ background is reduced by applying a cut on a topological discriminator which is based on computing the following projections:

$$P_\zeta = \left(\vec{p}_T^{\,e} + \vec{p}_T^{\,\mu} + \vec{p}_T^{\,miss}\right) \cdot \frac{\vec{\zeta}}{|\vec{\zeta}|} \qquad \text{and} \qquad P_\zeta^{vis} = \left(\vec{p}_T^{\,e} + \vec{p}_T^{\,\mu}\right) \cdot \frac{\vec{\zeta}}{|\vec{\zeta}|}, \tag{2}$$

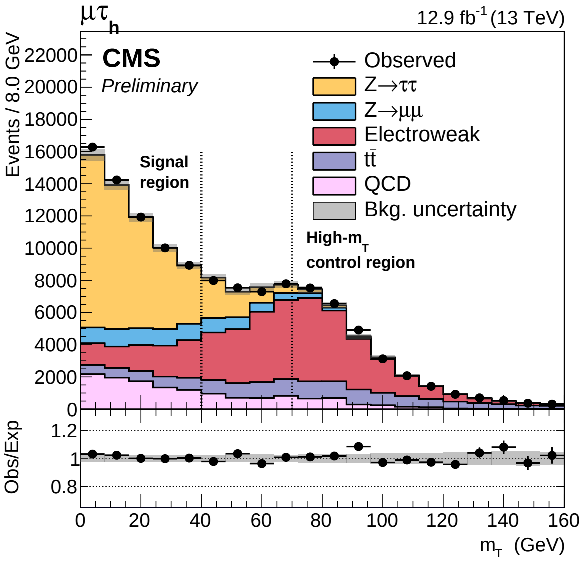

Figure 2: Distribution of the transverse mass variable for events in the $\mu\tau_h$ channel. The yields of all backgrounds are scaled following the final fit described in section 7, except for the W+jets background which is normalized using the high m_T region as indicated (see text). The "Bkg. uncertainty" band represents the systematic uncertainty on the background yield as determined in this fit in combination with the statistical uncertainty in each bin. The signal region is defined by $m_T < 40$ GeV as indicated, while the equivalent cut in the eτ_h channel is $m_T < 50$ GeV.

on the axis $\vec{\zeta}$ bisecting the directions $\vec{p}_T^{\,e}$ and $\vec{p}_T^{\,\mu}$ of the electron and muon momenta in the transverse plane. A cut of $D_\zeta = P_\zeta - 1.85 \cdot P_\zeta^{vis} > -20$ GeV is applied to events in the signal region. The distribution of this variable in eμ channel is shown in figure 3.

Finally, events are further categorized depending on the presence of a b tagged jet in the event. The "b–tag" category consists of events with at least one b tagged jet with p_T >20 GeV and $|\eta| < 2.4$ passing the medium working point of the CSV discriminator, and no more than one jet of any flavour with $p_T > 30$ GeV and $|\eta| < 4.7$. Events in the "no b–tag" category have exactly zero b tagged jets using the same definition, with no explicit requirement on jets of other flavour.

5 Background estimation

The irreducible $Z/\gamma^* \to \tau\tau$ background is present in all four channels in the low mass region. Data events in the $Z \to \mu\mu$ final state are used to calibrate the prediction from simulation. Imperfect modeling of events with high Z p_T is corrected by reweighting the shape of the MC simulation to the data in 2D bins of Z p_T and invariant mass. The acceptance of the category selections is calibrated by comparing the efficiency of the b–tag and no b–tag selections in the $Z/\gamma^* \to \tau\tau$ MC simulation and the $Z \to \mu\mu$ data. This is done by directly including $Z \to \mu\mu$ data in b–tag and no b–tag control regions in the final fit described in section 7.

Events with fake taus provide a large portion of the background in all four channels. The W+jets background is large in the $\mu\tau_h$ and eτ_h channels where the lepton comes from the W decay and the tau is provided by a jet. Events with high m_T are very pure in W+jets and provide a good control region in data. Fake taus also occur as a result of QCD multijet events. This background is fully estimated from data, making use of the fact that QCD events in which

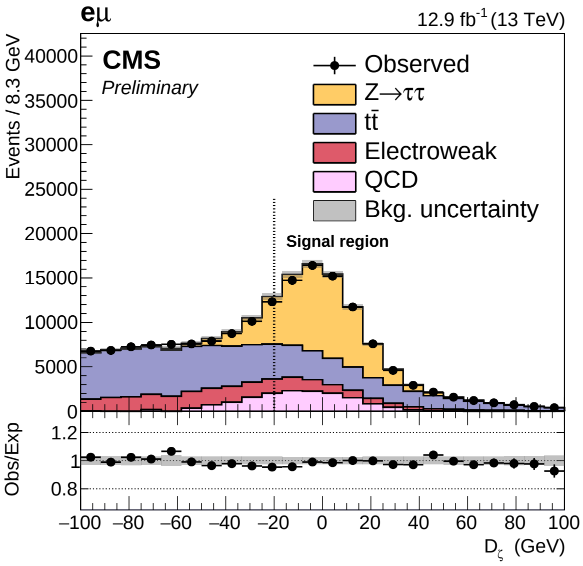

Figure 3: Distribution of the D_ζ variable for events in the eμ channel. The yields of all backgrounds are scaled following the final fit described in section 7. The "Bkg. uncertainty" band represents the systematic uncertainty on the background yield as determined in this fit in combination with the statistical uncertainty in each bin. The signal region is defined by $D_\zeta > -20$ GeV as indicated.

the candidate pair have opposite sign charges (OS) and same sign charges (SS) are similar and produced at approximately the same rate. A small fraction of QCD events have high m_T, and so the QCD and W backgrounds are estimated together making use of three control regions: OS with $m_\mathrm{T} > 70$ GeV, SS with $m_\mathrm{T} > 70$ GeV and SS with $m_\mathrm{T} < 50(40)$ GeV in the eτ_h ($\mu\tau_\mathrm{h}$) channels. These three control regions are included as a single bin in the final fit described in section 7 for the eτ_h and $\mu\tau_\mathrm{h}$ channels also applying the full b–tag and no b–tag category definitions, alongside the signal regions from all channels and categories.

The pre–fit predictions for the QCD and W backgrounds are found by subtracting the small number of other backgrounds from the data in the control region, and then assuming the remaining data to be from either W or QCD. The inputs of the OS/SS ratio for both W and QCD events and the extrapolation factor between high m_T and low m_T for the W background allow separation of the W and QCD predictions in all three control regions and the signal region. In the b–tag category, to account for low purity of W background in the b–tag category compared with tt̄, the b tagging requirement is removed from the category definition for the high m_T sidebands, and the additional extrapolation from this region to the full b–tag category is measured in MC simulation. The OS/SS ratio and the high m_T to low m_T extrapolation factor for the W are taken from MC simulation. The OS/SS ratio is found to be 4.4 ± 0.1 (4.7 ± 0.1) in $\mu\tau_\mathrm{h}$ (eτ_h) events in the no b–tag category and 4.0 ± 0.1 (4.2 ± 0.1) in the b–tag category without b tagging requirement. The value of this ratio is checked in data using a control region in which the tau is anti isolated, and found to be consistent within 8% for no b–tag events and 10% for b–tag events, which is then included in the final systematic uncertainties. The OS/SS ratio for QCD is measured by performing a fit in two sidebands in which the isolation of the electron/muon is loosened by different amounts. It is found to be 1.18 ± 0.04 for inclusive $\mu\tau_\mathrm{h}$ events and 1.02 ± 0.06 in inclusive eτ_h events. Additional uncertainties are included to cover the possible differences in this value in the b–tag category, the accurate measurement of which is made difficult by low statistics in the control region. The shape of the W+jets prediction is

	$\mu\tau_{\mathrm{h}}$	$\mathrm{e}\tau_{\mathrm{h}}$	$\tau_{\mathrm{h}}\tau_{\mathrm{h}}$	$\mathrm{e}\mu$
Trigger (threshold in GeV)	$\mu(22)$	$\mathrm{e}(25)$	$\tau_h(35)$ & $\tau_h(35)$	$\mu(8)$ & $\mathrm{e}(23)$ or $\mu(23)$ & $\mathrm{e}(12)$
Offline selection	$p_{\mathrm{T}}^{\mu} > 23$ GeV, $\lvert\eta^{\mu}\rvert < 2.1$ $p_{\mathrm{T}}^{\tau_h} > 30$ GeV, $\lvert\eta^{\tau_h}\rvert < 2.3$	$p_{\mathrm{T}}^{\mathrm{e}} > 26$ GeV, $\lvert\eta^{\mathrm{e}}\rvert < 2.1$ $p_{\mathrm{T}}^{\tau_h} > 30$ GeV, $\lvert\eta^{\tau_h}\rvert < 2.3$	$p_{\mathrm{T}}^{\tau_h} > 40$ GeV, $\lvert\eta^{\tau_h}\rvert < 2.1$ $p_{\mathrm{T}}^{\tau_h} > 40$ GeV, $\lvert\eta^{\tau_h}\rvert < 2.1$	$p_{\mathrm{T}}^{\mu} > 10(24)$ GeV, $\lvert\eta^{\mu}\rvert < 2.4$ $p_{\mathrm{T}}^{\mathrm{e}} > 13(24)$ GeV, $\lvert\eta^{\mathrm{e}}\rvert < 2.5$
Additional ID	Medium ID -	MVA ID 80% -	- -	Medium ID MVA ID 80%
Isolation	$I_{\mu}^{rel} < 0.15$ MVA Medium	$I_{\mathrm{e}}^{rel} < 0.1$ MVA Medium	MVA Tight MVA Tight	$I_{\mu}^{rel} < 0.2$ $I_{\mathrm{e}}^{rel} < 0.15$
Impact parameter (cm)	$d_{xy}^{\mu} < 0.045$ $d_{z}^{\mu} < 0.2$ $d_{z}^{\tau_h} < 0.2$	$d_{xy}^{\mathrm{e}} < 0.045$ $d_{z}^{\mathrm{e}} < 0.2$ $d_{z}^{\tau_h} < 0.2$	$d_{z}^{\tau_h} < 0.2$ $d_{z}^{\tau_h} < 0.2$	$d_{xy}^{\mu/\mathrm{e}} < 0.045$ $d_{z}^{\mu/\mathrm{e}} < 0.2$
Lepton vetoes	No loose $\mu^+\mu^-$ pair with $p_{\mathrm{T}}^{\mu} > 15$ GeV	No loose $\mathrm{e}^+\mathrm{e}^-$ pair with $p_{\mathrm{T}}^{\mathrm{e}} > 15$ GeV		-
	No additional loose e with $p_{\mathrm{T}} > 10$ GeV and $\lvert\eta\rvert < 2.5$ No additional loose μ with $p_{\mathrm{T}} > 10$ GeV and $\lvert\eta\rvert < 2.4$			

Table 1: Summary of the lepton selections in each channel. The candidates which are used to fire the trigger in each channel are indicated, as well as the p_{T} threshold which is required. In the eμ channel two triggers with complementary p_{T} thresholds are used, with a correspondingly higher offline p_{T} cut applied to the higher p_{T} leg (given in brackets). For the τ_h track impact parameter d_z the charged constituent with the highest p_{T} is used. The looser ID definitions used for the extra lepton vetoes are described in the text.

taken from MC simulation, while for the QCD the shape is taken from the SS low m_{T} control region.

In the $\tau_{\mathrm{h}}\tau_{\mathrm{h}}$ and eμ channels, the W+jets prediction is small and both shape and normalization are taken from MC simulation. The QCD background is sizable in both channels, in particular for $\tau_{\mathrm{h}}\tau_{\mathrm{h}}$. In the $\tau_{\mathrm{h}}\tau_{\mathrm{h}}$ channel the shape is taken from a sideband in which the isolation of the subleading tau is loosened. The definition of the sideband is optimized for each category balancing out two competing factors: the available statistics to obtain a smooth shape and the amount of extrapolation from the signal region definition. The normalization is found by scaling the prediction in the sideband by an extrapolation factor measured using SS events. The sideband for the no b–tag category is such that the leading tau passes the tight working point while the subleading tau passes the medium but not the tight working point. In the b–tag category the isolation on the subleading tau is loosened to passing loose but not tight working points, in order to obtain more statistics.

In the eμ channel the QCD estimate is obtained using the SS events. The OS/SS ratio is measured using a control region in data in which the electron has relative isolation $I_{\mathrm{e}}^{rel} > 0.15$ and/or the muon has relative isolation $I_{\mu}^{rel} > 0.2$ (to ensure orthogonality with the signal region) but both satisfy $I_{\ell}^{rel} < 0.4$. The OS/SS ratio is measured in bins of electron/muon p_{T} and ΔR between the electron and muon. An inclusive value of the OS/SS ratio is measured in the signal region selection using QCD MC simulation, and found to be 2.20 ± 0.32 - this is used to scale all the binned measurements to be consistent with this average. In the b–tag category the OS/SS ratio is found to be lower, measured to be 1.45 ± 0.12 in the data sideband. The statistics in the control regions in this category are too low to perform a measurement in bins of p_T and ΔR, but the values measured inclusively are corrected by a factor of 1.45/2.2 for events in the b–tag category to correct for this.

Background from $t\bar{t}$ events exists in all four channels, and is largest in the eμ channel. The prediction for both shape and normalization of this background is taken from MC simulation. A kinematic re-weighting is applied to the $t\bar{t}$ MC simulation to better match the top quark p_T distribution observed in data compared with the NNLO prediction [41, 42]. The shape and normalization of the background is then cross-checked in a control region in the eμ channel. The data/MC scale factor is found to be consistent with 1 within uncertainties, so no correction is applied to the normalization from MC simulation. The remaining backgrounds, which consist of diboson, $Z \rightarrow \ell\ell$ and single top are small in all channels and estimated from MC simulation, using the NLO cross-section predictions.

Where simulation is used, several data driven corrections are applied. The effect of the trigger is simulated by applying the trigger efficiencies measured in data to the MC simulation. Samples are also corrected for the any differences in electron and muon tracking, identification (ID) and isolation efficiency, measured using the tag–and–probe method [43] with $Z/\gamma^* \rightarrow ee$ and $Z/\gamma^* \rightarrow \mu\mu$ events in bins of p_T and η. Similarly a scale factor for the hadronic tau ID efficiency is measured using tag and probe and applied to MC simulation. The energies of jets in simulation are corrected to the generator level response of the jet and to compensate for pileup effects, using correction factors measured in bins of jet p_T and η. A correction is applied to the E_T^{miss} and its direction based on differences between measurements of hadronic recoil in $Z \rightarrow \mu\mu$ events in data and simulation - this is applied to the $Z \rightarrow \tau\tau$, W+jets and signal events. The efficiency for real and fake b jets to pass the medium working point of the CSV discriminator has been measured in data, using $t\bar{t}$ events for real b jets and Z/γ^*+jets events for light (mistag) jets. A data/MC scale factor is measured for these efficiencies and used to correct the number of b tagged jets in the MC simulation and hence the number of events in the b–tag and no b–tag categories. Corrections are applied to $Z \rightarrow \ell\ell$ events in the eτ_h and $\tau_h\tau_h$ channels in which an electron is reconstructed as a hadronic tau, and in $Z \rightarrow \ell\ell$ events in the $\mu\tau_h$ and $\tau_h\tau_h$ channels in which a muon is reconstructed as a hadronic tau, to account for measured differences in $\ell \rightarrow$tau fake rate in data and MC simulation.

Figure 4 illustrates the full set of control and signal regions which are included in the final fit. In the case of the control regions, the background which is most constrained by the region is illustrated by the colour of the shading, following the conventions of the other figures in this report. Note that the control regions are included as a single bin, whereas full binned shapes are used for the signal regions.

6 Systematic uncertainties

A number of systematic uncertainties are considered which affect the normalization and/or shape of a given process.

Normalization uncertainties:

- The uncertainty on the integrated luminosity has been measured to be 6.2% [44]. This is applied to all backgrounds estimated from simulation.
- As described in section 5, MC simulation is corrected for measured differences in ID and isolation efficiency in data and MC simulation as a function of p_T and η. Additionally the efficiencies of the trigger measured in data are applied to the MC

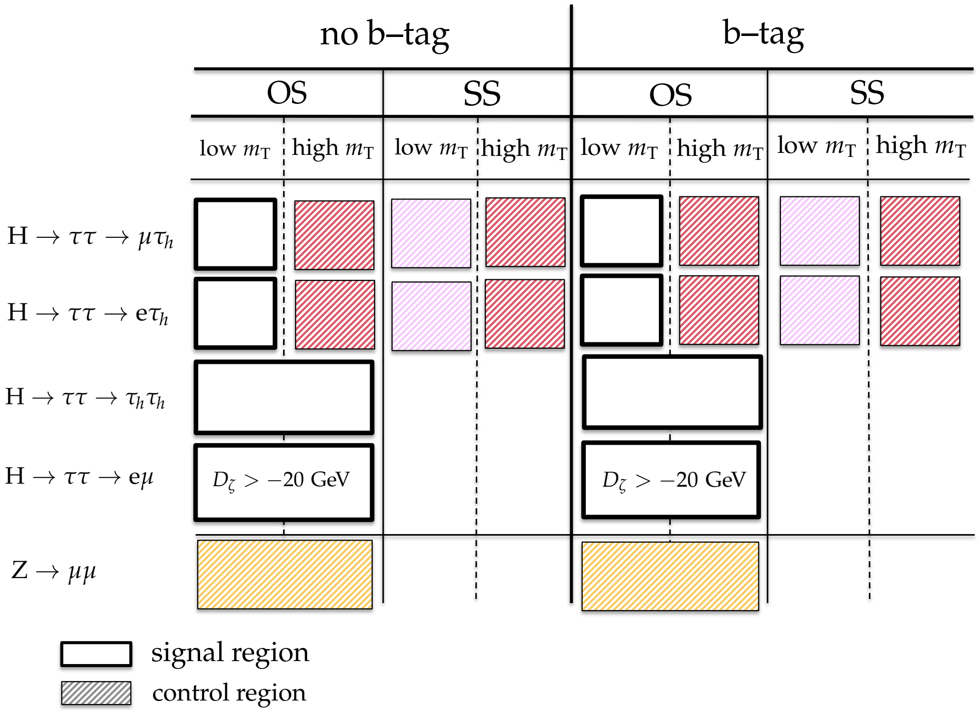

Figure 4: Illustration of the full set of signal and control regions which are included in the final fit for this analysis described in section 7. In the case of the control regions, the colour indicates which background is most constrained by the region.

simulation. Uncertainties on these measurements are found to be 2% for electrons and muons, and this is applied as a systematic to signal and all simulated backgrounds. Similarly the uncertainty on the tau ID efficiency measurement is 6%. This is applied as 5% which is fully correlated between the channels and 3% (9.2%) uncorrelated in the $e\tau_h$ and $\mu\tau_h$ ($\tau_h\tau_h$) channels, to account for the parts of the tau ID which differ. In the $\tau_h\tau_h$ channel an uncertainty on the tau trigger efficiency of 7% is included in the uncorrelated part. These uncertainties are applied to the $Z/\gamma^* \to \tau\tau$ background and the components of the $t\bar{t}$ and diboson backgrounds which contain real taus, as well as the signal, in all signal and control regions.

- The uncertainty on the jet energy scale has an effect on the number of events which enter each category, and is applied for all backgrounds where the normalization is taken from simulation, in all signal and control regions. The size of the uncertainty varies in the range 1-10%.
- The uncertainties on the rates of jets passing the b tagging discriminator, both for real b jets and mistagged jets, are applied to all simulated backgrounds in all signal and control regions. The size of the uncertainty varies in the range 1-5%.
- An uncertainty on the resolution and response of the E_T^{miss} is derived in studies of the hadronic recoil in $Z \to \mu\mu$ events in data and MC simulation. This amounts to a $1-3\%$ normalization uncertainty, and is applied to all signal and control regions.
- The uncertainty on the normalization of the $Z/\gamma^* \to \tau\tau$ and $Z/\gamma^* \to \ell\ell$ amounts to 4% due to the theoretical uncertainty on the NNLO cross-section. Similarly the un-

certainty on the diboson and single top contribution is 5%. For the $t\bar{t}$ background the cross-section uncertainty is 6%. In the $e\mu$ and $\tau_h\tau_h$ channels and the $Z \rightarrow \mu\mu$ control region where the normalization of the W background is taken from MC simulation, the applied cross-section uncertainty is 4%.

- Uncertainties on the measurements of the rate at which electrons and muons are reconstructed as taus are included. An uncertainty of 30% is applied to the component of the $Z/\gamma^* \rightarrow \ell\ell$ background in which an electron is reconstructed as a tau in the $e\tau_h$ channel. In the $\tau_h\tau_h$ channel a different working point is used for the anti-electron discrminator and the uncertainty on this component is found to be 10%. In the $\mu\tau_h$ ($\tau_h\tau_h$) channel the uncertainty for a muon being reconstructed as a tau is 30% (20%).
- For the remaining $Z/\gamma^* \rightarrow \ell\ell$ events in which a jet is reconstructed as a tau, an uncertainty of 20% is applied. This uncertainty is also included on the $t\bar{t}$ background for events in which a jet fakes a tau.
- The systematic uncertainty on the QCD OS/SS ratio affects the QCD normalization in the high m_T OS events and in the signal region, and amounts to 4% (12%) in no b–tag category and 60% (60%) in b–tag for the $\mu\tau_h$ ($e\tau_h$) channels.
- The systematic uncertainty on the W OS/SS ratio affects the W normalization in the signal region and the OS high $\mathrm{m_T}$ control region and amounts to 8% (10%) in the no b–tag (b–tag) category in both the $e\tau_h$ and $\mu\tau_h$ channels, while the statistical uncertainty amounts to 2% (2%) in the no b–tag category and 11% (14%) in the b–tag category in the $\mu\tau_h$ ($e\tau_h$) channel.
- The statistical uncertainty on the high m_T to low m_T extrapolation factor affects the W normalization in both the SS QCD control region and the signal region and amounts to 2% (2%) in the no b–tag category and 14% (17%) in b–tag category for the $\mu\tau_h$ ($e\tau_h$) channel. A systematic uncertainty of 20% is also applied in both categories and channels.
- For the $\tau_h\tau_h$ channel, the uncertainty on the QCD estimate is 2% in the no b–tag category and 20% in the b–tag category, taking into account the available statistics in the control region and the statistical uncertainty on the extrapolation factor measured in SS data. An additional systematic uncertainty of 12% in no b–tag and 14% in b–tag is included to cover differences due to choice of anti-isolated sideband.
- In the $e\mu$ channel, an uncertainty of 23% on the QCD background is applied in the no b–tag category and 34% in the b–tag category, including the uncertainty on the measured OS/SS factor, found by comparing the inclusive measurements in the signal region and sideband in QCD MC simulation.
- An uncertainty is applied on the $Z/\gamma^* \rightarrow \tau\tau$ process to cover potential extrapolation from $Z \rightarrow \mu\mu$ events to $Z/\gamma^* \rightarrow \tau\tau$ events when including the $Z \rightarrow \mu\mu$ events in the fit as a control region. This amounts to 2% in no b–tag and 5% in b–tag.
- In the case of the model dependent limits, theory uncertainties are included on the signal predictions. Uncertainties due to the different choices of factorization and renormalization scales are included. The MSTW2008 [45] parton distribution functions are used and the recommended prescription [45, 46] to compute the uncertainties is followed. Uncertainties are evaluated separately for each m_A - $\tan\beta$ point and typically vary between 15 and 25%.
- Also for the model dependent limits theory uncertainties are included on the SM Higgs boson prediction. Uncertainties due to different choices of renormalization

and factorization scales are included, and amount to 3.9% for gluon fusion signal, 0.4% for VBF, 2.8% for ZH and 0.5% for WH. Uncertainties due to the PDF and α_s amount to 3.2% for gluon fusion, 2.1% for VBF, 1.6% for ZH and 1.9% for WH. More information can be found in [47].

Shape uncertainties:

- In order to account for the necessary extrapolation of the tag and probe measurement of the tau ID efficiency, which mostly consists of taus close to the Z peak, to the higher p_{T} taus in the high mass signal, an additional uncertainty is applied. The size of the uncertainty is 20% of the tau p_{T} in TeV. This has a direct effect on the total transverse mass shape and hence is included as a shape uncertainty.
- The uncertainty on the reweighting of the $\mathrm{t\bar{t}}$ samples based on top quark p_{T}, as described in section 5, is included as a shape uncertainty with the size of 100% of the correction.
- The uncertainty on the shape reweighting of $\mathrm{Z} \to \tau\tau$ events as measured in $\mathrm{Z} \to \mu\mu$ events is included as 100% of the correction.
- The uncertainty on the tau energy scale in MC simulation is 3% and affects both the yield and shape of the final distribution in the $\mathrm{e}\tau_{\mathrm{h}}$, $\mu\tau_{\mathrm{h}}$ and $\tau_{\mathrm{h}}\tau_{\mathrm{h}}$ channels. This is included as a shape uncertainty on the $\mathrm{Z}/\gamma^* \to \tau\tau$ background, and the portions of the $\mathrm{t\bar{t}}$ and diboson backgrounds containing real taus, as well as the signal.
- In the $\mathrm{e}\mu$ channel, shape uncertainties for the electron energy scale are included which correspond to a 1% uncertainty in the barrel and 2.5% in the endcaps.
- A shape uncertainty is included on the W+jets background corresponding to 100% of the maximal variation in data/MC for the jet→tau fake rate as a function of jet p_{T}.

Both the normalization and shape systematics are incorporated in the fit described in section 7 via nuisance parameters.

7 Results

The total transverse mass is the final discriminating variable used to search for an excess due to signal. It is defined as:

$$m_{\mathrm{T}}^{\mathrm{tot}} = \sqrt{m_{\mathrm{T}}(E_{\mathrm{T}}^{\mathrm{miss}}, \tau_1^{\mathrm{vis}})^2 + m_{\mathrm{T}}(E_{\mathrm{T}}^{\mathrm{miss}}, \tau_2^{\mathrm{vis}})^2 + m_{\mathrm{T}}(\tau_1^{\mathrm{vis}}, \tau_2^{\mathrm{vis}})^2}. \tag{3}$$

In this equation, the transverse mass between two objects 1 and 2 is given by:

$$m_{\mathrm{T}}(1,2) = \sqrt{2p_{\mathrm{T}}(1)p_{\mathrm{T}}(2)(1-\cos\Delta\phi(1,2))}, \tag{4}$$

and hence $m_{\mathrm{T}}(E_{\mathrm{T}}^{\mathrm{miss}}, \tau_1^{\mathrm{vis}})$ is equivalent to the transverse mass defined in equation 1 for the $\mu\tau_{\mathrm{h}}$ and $\mathrm{e}\tau_{\mathrm{h}}$ channels.

This variable was first used by ATLAS in MSSM $\phi \to \tau\tau$ searches [21] and increases the separation between signal and QCD in the $\mathrm{e}\tau_{\mathrm{h}}$, $\mu\tau_{\mathrm{h}}$ and $\tau_{\mathrm{h}}\tau_{\mathrm{h}}$ channels compared with the full ditau mass. It was also found to have improved separation between signal and $\mathrm{t\bar{t}}$ in the $\mathrm{e}\mu$ channel compared with the SVFit transverse mass used in [22].

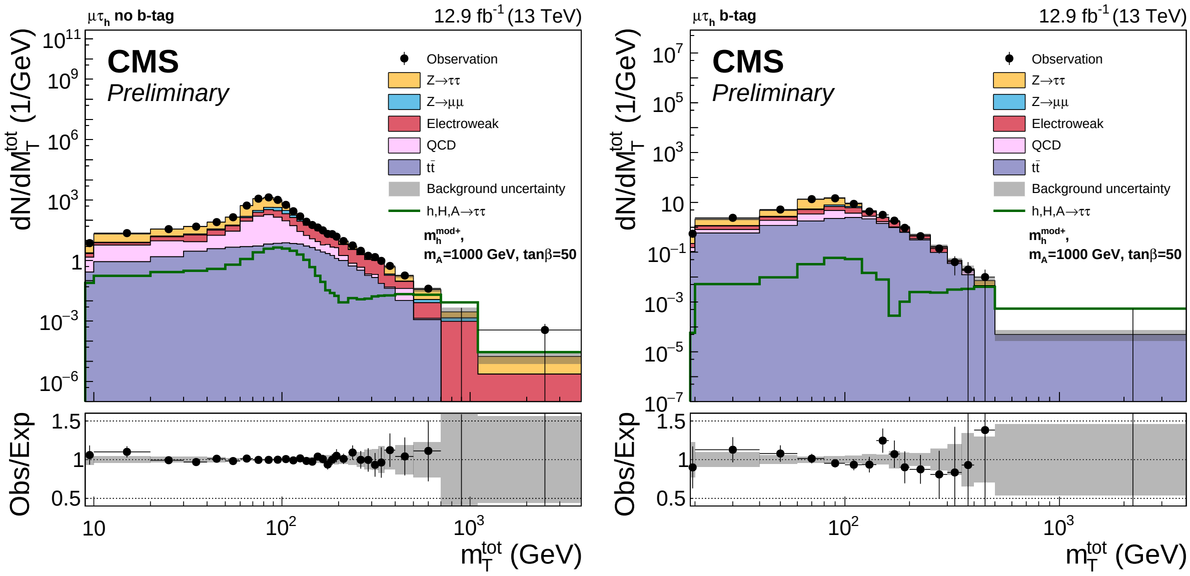

(a)

(b)

Figure 5: Post–fit plot of the total transverse mass distribution in (a) the no b–tag category and (b) the b–tag category of the $\mu\tau_h$ channel

The binned distributions of total transverse mass are fitted simultaneously in all four channels and the b–tag and no b–tag categories, using a binned maximum likelihood fit. The tools used for fitting are based on ROOSTATS [48]. For the $e\tau_\mathrm{h}$ and $\mu\tau_\mathrm{h}$ channels the additional control regions described in section 5 are also included in the fit as single bins.

The total transverse mass distributions for the b–tag and no b–tag categories in the different channels can be seen in figures 5-8. These plots are made following the fit to data, and the uncertainty band includes the full set of post–fit systematic uncertainties. Note that the signal shown on these plots is for a benchmark point in the $m_\mathrm{h}^{\mathrm{mod}+}$ scenario corresponding to $m_\mathrm{A} = 1000\,\mathrm{GeV}$ and $\tan\beta = 50$, and consists of the combination of the predictions for the three neutral Higgs bosons.

Upper limits are set at the 95% confidence level (CL) on the the cross-section times branching fraction for the two dominant production modes, gluon fusion (ggϕ) and b-associated production (bbϕ). The limits are set assuming a single resonance signal with narrow width. Figure 9 shows these limits as a function of Higgs boson mass m_ϕ. Limits are set using the asymptotic approximation, where the background-only prediction consists of the sum of all backgrounds and no SM-like Higgs boson. This choice of null hypothesis is made such that the results are truly model independent and more easily recast in different BSM scenarios containing a given choice of Higgs sector. In this procedure when a limit is set on one MSSM signal process the alternative signal process is “profiled”, meaning that it is allowed to float as a nuisance in the fit. In general the sensitivity of the limit on ggϕ signal is dominated by the no b–tag category where almost all of the ggϕ signal falls, whereas both categories contribute to the limit on bbϕ due to the fact that a large portion of the bbϕ signal falls in the no b–tag category, due to the fact that the b–jets in the signal tend to be soft and can often fall outside the acceptance. Figure 10 shows the comparison of the expected limits on each signal for the different channels, to illustrate the contribution of each to the final sensitivity.

A two dimensional likelihood scan of the cross-section times branching fraction for the ggϕ

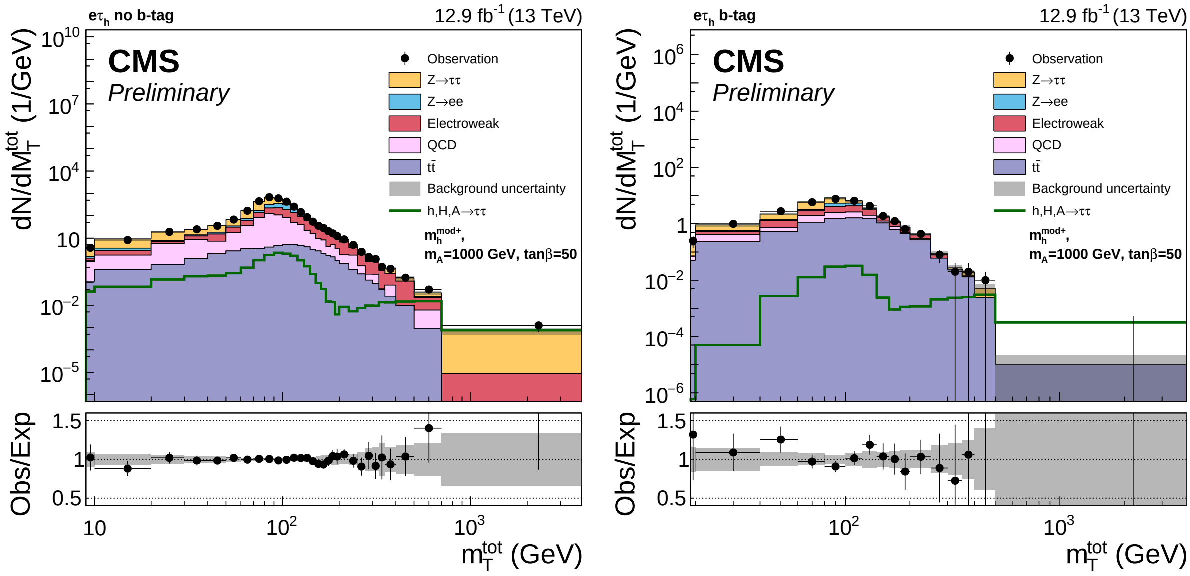

(a) (b)

Figure 6: Post–fit plot of the total transverse mass distribution in (a) the no b–tag category and (b) the b–tag category of the $e\tau_h$ channel

and bbϕ processes is also provided. Each signal mass point is tested and the best fit point compared with the 1 and 2 sigma contours under the assumption that any fitted signal cross-section should be positive or zero. Also shown is the best fit value in the case of using an Asimov dataset containing background plus 125 GeV SM Higgs boson, to illustrate the effect our sensitivity to the SM Higgs boson could have on these results. The results can be seen in figure 11.

Limits are also set on m_{A} and tanβ in two different benchmark models; the $m_{\mathrm{h}}^{\mathrm{mod+}}$ and hMSSM scenarios. The neutral MSSM Higgs boson production cross sections and the corresponding uncertainties are provided by the LHC Higgs Cross Section Group [47, 49]. The program SusHi [50] (v1.4.1) has been used to calculate cross-sections for the gluon fusion process. This includes NLO (supersymmetric)-QCD corrections [51–56], NNLO QCD corrections for the top-quark contribution in the effective theory of a heavy top-quark [57–61] and electroweak effects by light quarks [62, 63]. For the bbϕ process, the four-flavor NLO QCD calculation [64, 65] and the five-flavor NNLO QCD calculation, as implemented in SusHi based on BBH@NNLO [66] have been combined using the Santander matching scheme [67]. Higgs masses and mixing and effective Yukawa couplings have been calculated with FeynHiggs [68–72] (v2.10.2 with default flags), except for the hMSSM. The Higgs boson branching fraction to tau leptons in the different benchmark scenarios has been obtained with FeynHiggs for the $m_{\mathrm{h}}^{\mathrm{mod+}}$ scenario and HDECAY [73] (v6.40) for hMSSM. The hMSSM scenario is strictly only valid for $m_{\mathrm{A}} > 130$ GeV and tan$\beta < 10$ - model predictions are still calculated for points up to tan$\beta = 60$, but it should be noted that direct higher order SUSY corrections to down-type fermion couplings (also known as $\Delta\beta$ corrections), and corrections due to SUSY particles in loops are neglected.

A statistical procedure is used for the model dependent results which allows differentiation between the possibility of SM and MSSM Higgs boson sector [19]. A test of the compatibility of the data with the background plus a signal with the three neutral Higgs bosons h, H and A compared to a signal with an SM Higgs boson of mass 125 GeV is performed, and limits

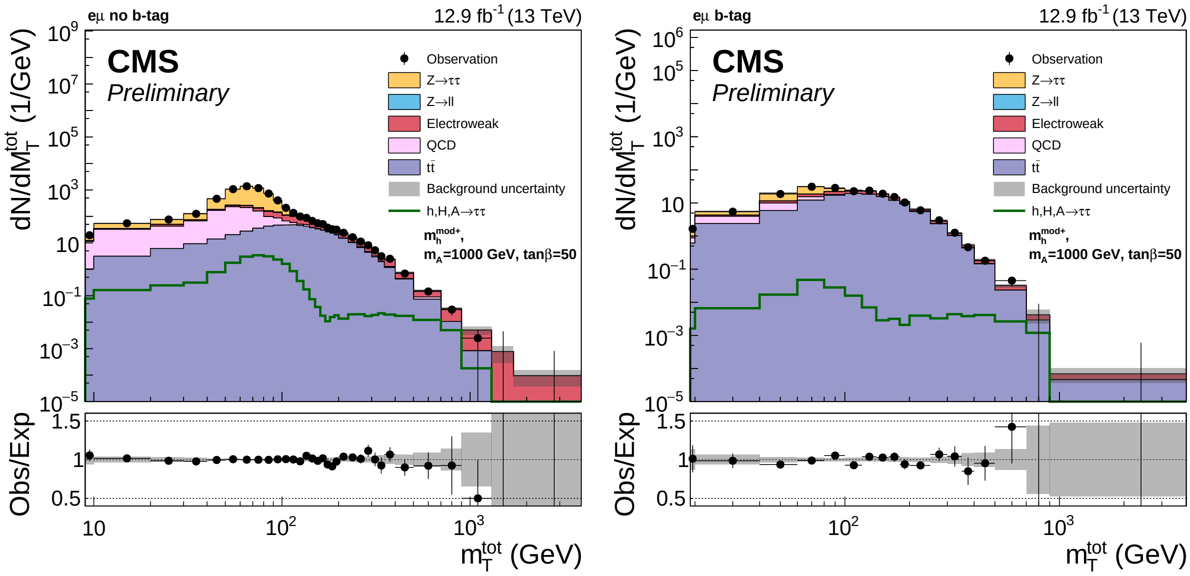

(a) (b)

Figure 7: Post–fit plot of the total transverse mass distribution in (a) the no b–tag category and (b) the b–tag category of the $e\mu$ channel

on tanβ vs m_A are then set corresponding to the 95% CL exclusion. The results are shown in figure 12 for the two scenarios.

8 Summary

A search for neutral Higgs bosons of the MSSM decaying into the $\tau\tau$ final state has been presented, using the $\mu\tau_h$, $e\tau_h$, $\tau_h\tau_h$ and $e\mu$ final states. The dataset corresponds to an integrated luminosity of 12.9 fb^{-1}, recorded by the CMS detector at 13 TeV centre–of–mass energy in 2016. No evidence for a signal has been found and exclusion limits on the production cross section times branching fraction for the gluon fusion and b-associated production processes are presented. The results are also interpreted in the context of two MSSM benchmark scenarios, where exclusions are set as a function of m_A and tanβ.

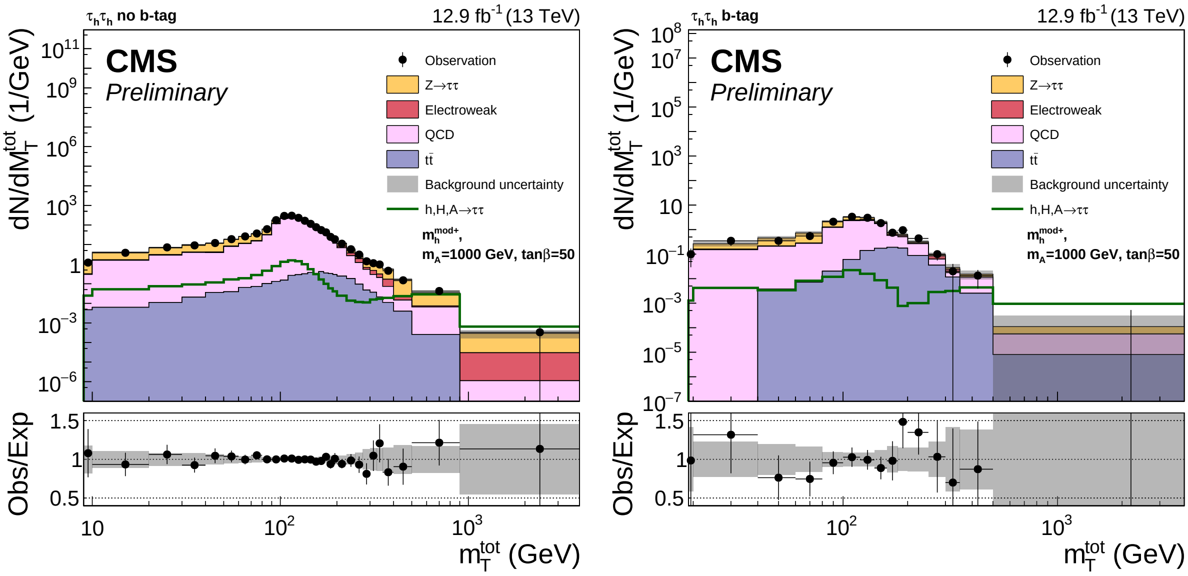

(a)

(b)

Figure 8: Post–fit plot of the total transverse mass distribution in (a) the no b–tag category and (b) the b–tag category of the $\tau_h\tau_h$ channel

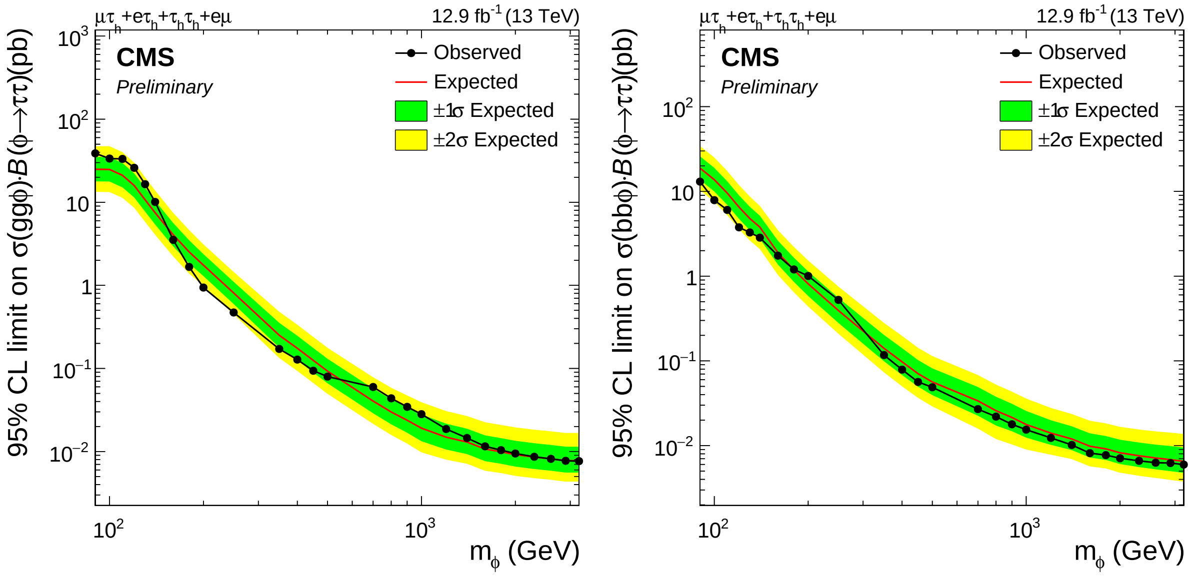

(a)

(b)

Figure 9: Expected and observed limits on cross-section times branching fraction for a) the gluon fusion process ($gg\phi$) and b) the b–associated production process ($bb\phi$), resulting from the combination of all four channels. The narrow width approximation is used for the signal.

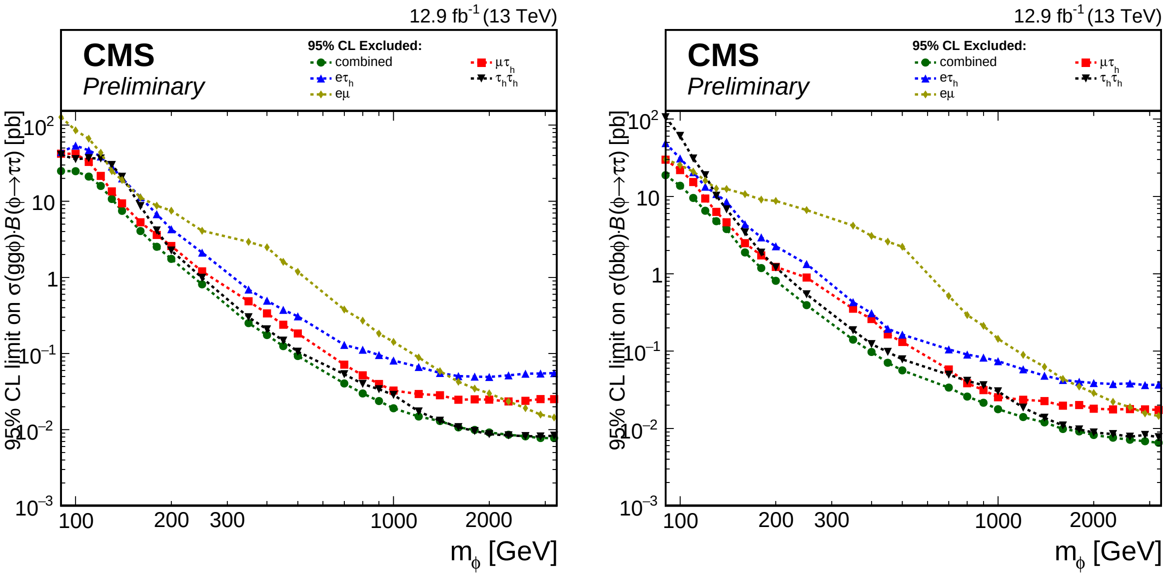

(a)

(b)

Figure 10: Comparison between the expected limits on cross-section times branching fraction for a) the gluon fusion process (ggϕ) and b) the b–associated production process (bbϕ) in each final state channel.

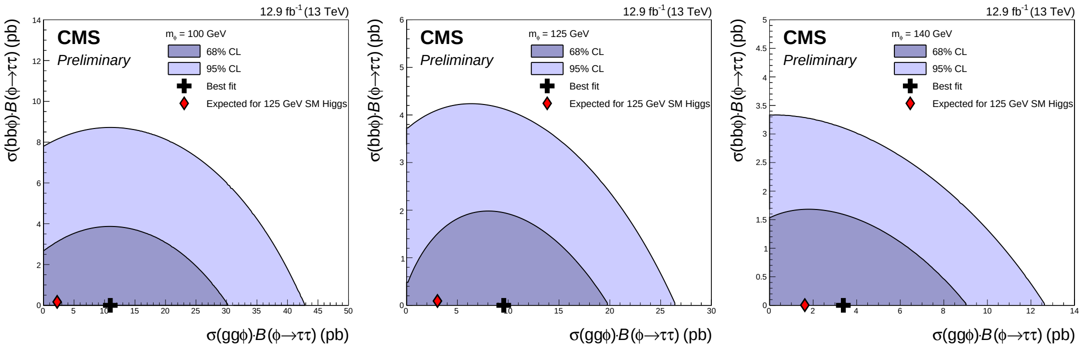

(a) $m_\phi = 100$ GeV (b) $m_\phi = 125$ GeV (c) $m_\phi = 140$ GeV

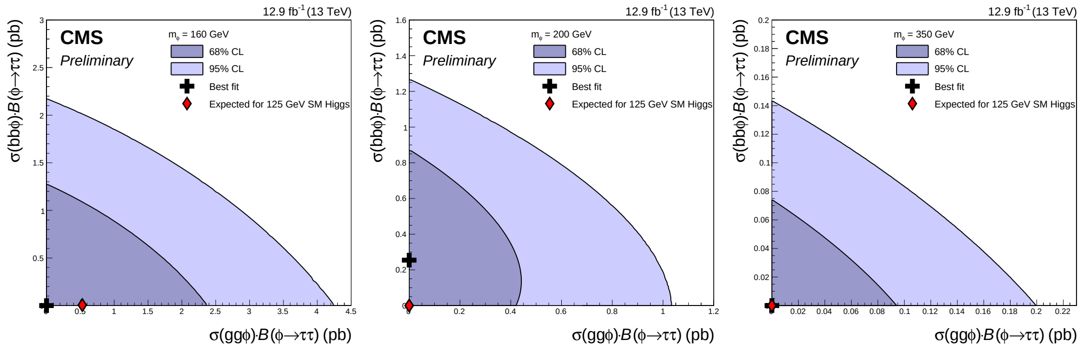

(d) $m_\phi = 160$ GeV (e) $m_\phi = 200$ GeV (f) $m_\phi = 350$ GeV

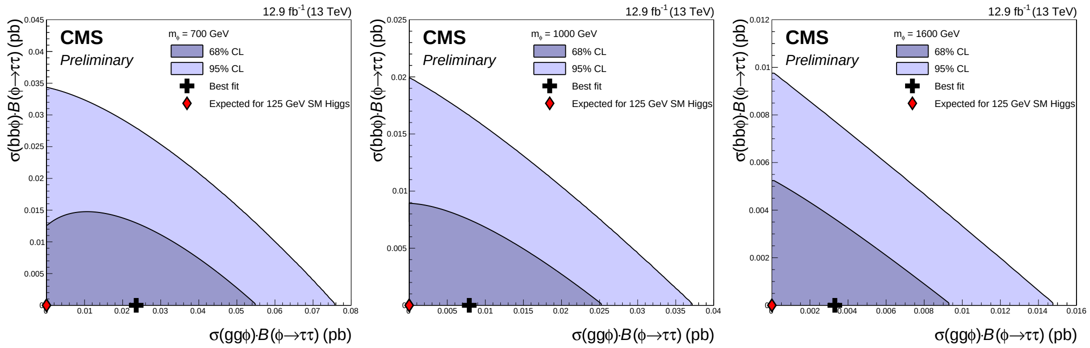

(g) $m_\phi = 700$ GeV (h) $m_\phi = 1000$ GeV (i) $m_\phi = 1600$ GeV

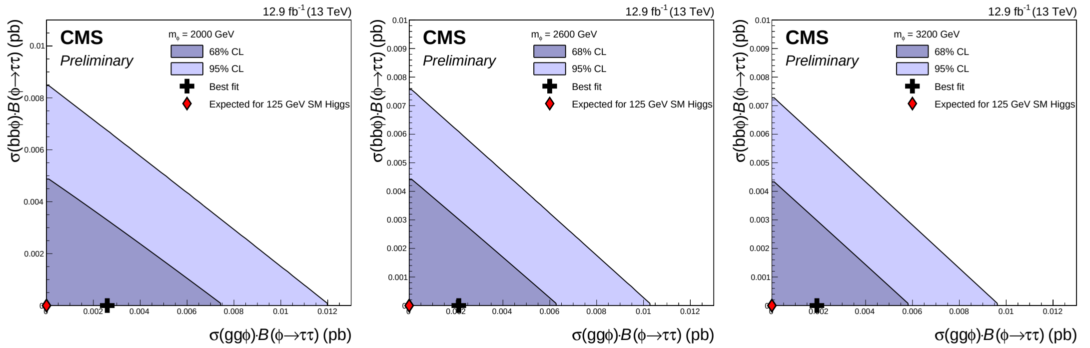

(j) $m_\phi = 2000$ GeV (k) $m_\phi = 2600$ GeV (l) $m_\phi = 3200$ GeV

Figure 11: 2D likelihood scan of cross-section time branching fraction for ggϕ vs bbϕ production processes, for selected Higgs boson masses between 100 GeV and 3200 GeV. The best fit point (black cross) and the 1 and 2 sigma contours are shown for the observed data. Also shown is the best fit value for an Asimov dataset containing background plus the SM Higgs with mass 125 GeV (red diamond).

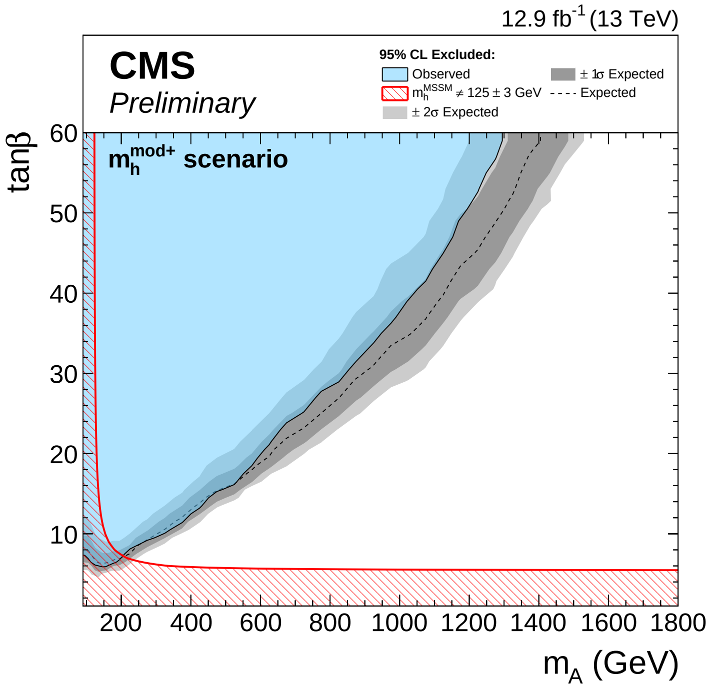

(a) m_h^{mod+}

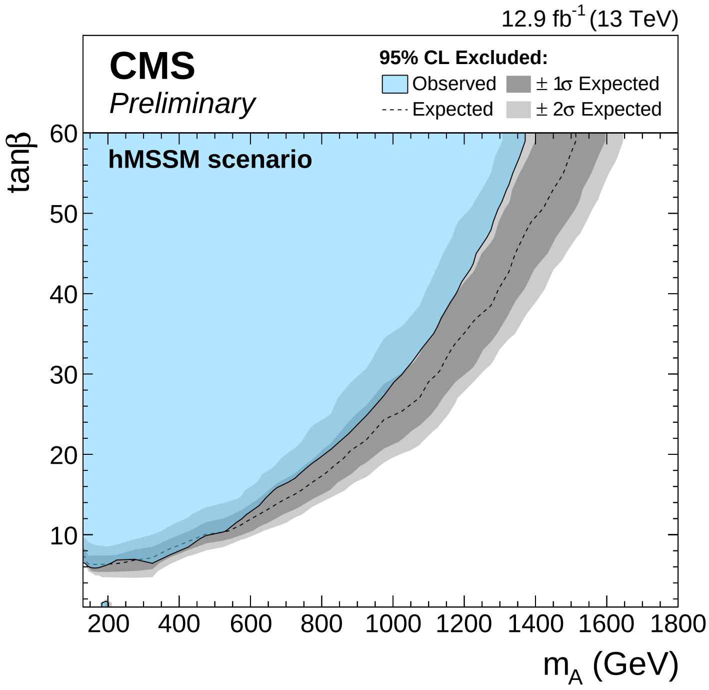

(b) hMSSM

Figure 12: Model dependent exclusion limits in the m_A-tan β plane, combining all channels, for a) the m_h^{mod+} and b) hMSSM scenarios. In a) the red contour indicates the region which does not yield a Higgs boson consistent with a mass of 125 GeV within the theoretical uncertainties of ±3 GeV.

References

[1] ATLAS Collaboration, "Observation of a new particle in the search for the Standard Model Higgs boson with the ATLAS detector at the LHC", *Phys. Lett. B* **716** (2012) 1–29, `doi:10.1016/j.physletb.2012.08.020`, `arXiv:1207.7214`.

[2] CMS Collaboration, "Observation of a new boson at a mass of 125 GeV with the CMS experiment at the LHC", *Phys. Lett. B* **716** (2012) 30–61, `doi:10.1016/j.physletb.2012.08.021`, `arXiv:1207.7235`.

[3] F. Englert and R. Brout, "Broken Symmetry and the Mass of Gauge Vector Mesons", *Phys. Rev. Lett.* **13** (1964) 321, `doi:10.1103/PhysRevLett.13.321`.

[4] P. W. Higgs, "Broken symmetries, massless particles and gauge fields", *Phys. Lett.* **12** (1964) 132, `doi:10.1016/0031-9163(64)91136-9`.

[5] P. W. Higgs, "Broken Symmetries and the Masses of Gauge Bosons", *Phys. Rev. Lett.* **13** (1964) 508, `doi:10.1103/PhysRevLett.13.508`.

[6] G. S. Guralnik, C. R. Hagen, and T. W. B. Kibble, "Global Conservation Laws and Massless Particles", *Phys. Rev. Lett.* **13** (1964) 585, `doi:10.1103/PhysRevLett.13.585`.

[7] P. W. Higgs, "Spontaneous Symmetry Breakdown without Massless Bosons", *Phys. Rev.* **145** (1966) 1156, `doi:10.1103/PhysRev.145.1156`.

[8] T. W. B. Kibble, "Symmetry breaking in non-Abelian gauge theories", *Phys. Rev.* **155** (1967) 1554, `doi:10.1103/PhysRev.155.1554`.

[9] ATLAS, CMS Collaboration, "Combined Measurement of the Higgs Boson Mass in pp Collisions at $\sqrt{s} = 7$ and 8 TeV with the ATLAS and CMS Experiments", *Phys. Rev. Lett.* **114** (2015) 191803, `doi:10.1103/PhysRevLett.114.191803`, `arXiv:1503.07589`.

[10] ATLAS, CMS Collaboration, "Measurements of the Higgs boson production and decay rates and constraints on its couplings from a combined ATLAS and CMS analysis of the LHC pp collision data at $\sqrt{s} = 7$ and 8 TeV", *JHEP* **08** (2016) 045, `doi:10.1007/JHEP08(2016)045`, `arXiv:1606.02266`.

[11] ATLAS Collaboration, "Study of the spin and parity of the Higgs boson in diboson decays with the ATLAS detector", *Eur. Phys. J. C.* **75** (2015), no. 10, 476, `doi:10.1140/epjc/s10052-015-3685-1`, `arXiv:1506.05669`.

[12] CMS Collaboration, "Constraints on the spin-parity and anomalous HVV couplings of the Higgs boson in proton collisions at 7 and 8 TeV", *Phys. Rev. D* **92** (2015), no. 1, 012004, `doi:10.1103/PhysRevD.92.012004`, `arXiv:1411.3441`.

[13] A. Djouadi, "The Anatomy of electro-weak symmetry breaking. II. The Higgs bosons in the minimal supersymmetric model", *Phys. Rept.* **459** (2008) 1–241, `doi:10.1016/j.physrep.2007.10.005`, `arXiv:hep-ph/0503173`.

[14] G. C. Branco et al., "Theory and phenomenology of two-Higgs-doublet models", *Phys. Rept.* **516** (2012) 1–102, `doi:10.1016/j.physrep.2012.02.002`, `arXiv:1106.0034`.

[15] Y. A. Golfand and E. P. Likhtman, "Extension of the Algebra of Poincare Group Generators and Violation of p Invariance", *JETP Lett.* **13** (1971) 323.

[16] J. Wess and B. Zumino, "Supergauge transformations in four dimensions", *Nucl. Phys. B.* **70** (1974) 39, `doi:10.1016/0550-3213(74)90355-1`.

[17] M. Carena et al., "MSSM Higgs Boson Searches at the LHC: Benchmark Scenarios after the Discovery of a Higgs-like Particle", *Eur. Phys. J. C.* **73** (2013), no. 9, 2552, `doi:10.1140/epjc/s10052-013-2552-1`, `arXiv:1302.7033`.

[18] E. Bagnaschi et al., "Benchmark scenarios for low tan β in the MSSM", Technical Report LHCHXSWG-2015-002, CERN, Geneva, Aug, 2015.

[19] CMS Collaboration, "Search for neutral MSSM Higgs bosons decaying to a pair of tau leptons in pp collisions", *JHEP* **10** (2014) 160, `doi:10.1007/JHEP10(2014)160`, `arXiv:1408.3316`.

[20] CMS Collaboration, "Search for additional neutral Higgs bosons decaying to a pair of tau leptons in pp collisions at $\sqrt{s} = 7$ and 8 TeV", CMS Physics Analysis Summary CMS-PAS-HIG-14-029, CERN, Geneva, 2015.

[21] ATLAS Collaboration, "Search for neutral Higgs bosons of the minimal supersymmetric standard model in pp collisions at $\sqrt{s}$ = 8 TeV with the ATLAS detector", *JHEP* **11** (2014) 056, `doi:10.1007/JHEP11(2014)056`, `arXiv:1409.6064`.

[22] CMS Collaboration, "Search for a neutral MSSM Higgs boson decaying into $\tau\tau$ at 13 TeV", CMS Physics Analysis Summary CMS-PAS-HIG-16-006, CERN, 2016.

[23] ATLAS Collaboration, "Search for Minimal Supersymmetric Standard Model Higgs bosons H/A and for a Z' boson in the $\tau\tau$ final state produced in pp collisions at $\sqrt{s} = 13$ TeV with the ATLAS Detector", *Eur. Phys. J. C.* **76** (2016), no. 11, 585, `doi:10.1140/epjc/s10052-016-4400-6`, `arXiv:1608.00890`.

[24] ATLAS Collaboration, "Search for Minimal Supersymmetric Standard Model Higgs Bosons H/A in the $\tau\tau$ final state in up to 13.3 fb^{-1} of pp collisions at $\sqrt{s}$= 13 TeV with the ATLAS Detector", ATLAS Conference Note ATLAS-CONF-2016-085, 2016.

[25] CMS Collaboration, "The CMS experiment at the CERN LHC", *JINST* **3** (2008) S08004, `doi:10.1088/1748-0221/3/08/S08004`.

[26] CMS Collaboration, "Particle–Flow Event Reconstruction in CMS and Performance for Jets, Taus, and $E_{\mathrm{T}}^{\mathrm{miss}}$", CMS Physics Analysis Summary CMS-PAS-PFT-09-001, 2009.

[27] CMS Collaboration, "Commissioning of the Particle-flow Event Reconstruction with the first LHC collisions recorded in the CMS detector", CMS Physics Analysis Summary CMS-PAS-PFT-10-001, 2010.

[28] K. Rose, "Deterministic annealing for clustering, compression, classification, regression, and related optimization problems", *Proceedings of the IEEE* **86** (Nov, 1998) 2210–2239, `doi:10.1109/5.726788`.

[29] CMS Collaboration, "Performance of electron reconstruction and selection with the CMS detector in proton-proton collisions at s = 8 TeV", *JINST* **10** (2015) P06005, `doi:10.1088/1748-0221/10/06/P06005`, `arXiv:1502.02701`.

[30] H. Voss, A. Höcker, J. Stelzer, and F. Tegenfeldt, "TMVA, the Toolkit for Multivariate Data Analysis with ROOT", in *XIth International Workshop on Advanced Computing and Analysis Techniques in Physics Research (ACAT)*, p. 40. 2007. `arXiv:physics/0703039`.

[31] CMS Collaboration, "Performance of CMS muon reconstruction in pp collision events at $\sqrt{s} = 7$ TeV", *JINST* **7** (2012) P10002, `doi:10.1088/1748-0221/7/10/P10002`, `arXiv:1206.4071`.

[32] M. Cacciari, G. P. Salam, and G. Soyez, "FastJet user manual", *Eur. Phys. J. C.* **72** (2012) 1896, `doi:10.1140/epjc/s10052-012-1896-2`, `arXiv:1111.6097`.

[33] M. Cacciari and G. P. Salam, "Dispelling the N^3 myth for the k_t jet-finder", *Phys. Lett. B* **641** (2006) 57, `doi:10.1016/j.physletb.2006.08.037`, `arXiv:hep-ph/0512210`.

[34] CMS Collaboration, "Identification of b-quark jets with the CMS experiment", *JINST* **8** (2013) P04013, `doi:10.1088/1748-0221/8/04/P04013`, `arXiv:1211.4462`.

[35] CMS Collaboration, "Performance of reconstruction and identification of tau leptons in their decays to hadrons and tau neutrino in LHC Run-2", Technical Report CMS-PAS-TAU-16-002, CERN, Geneva, 2016.

[36] CMS Collaboration, "Reconstruction and identification of lepton decays to hadrons and at CMS", *JINST* **11** (2016), no. 01, P01019, `doi:10.1088/1748-0221/11/01/P01019`, `arXiv:1510.07488`.

[37] CMS Collaboration, "Performance of the CMS missing transverse momentum reconstruction in pp data at $\sqrt{s}$ = 8 TeV", *JINST* **10** (2015) P02006, `doi:10.1088/1748-0221/10/02/P02006`, `arXiv:1411.0511`.

[38] T. Sjostrand, S. Mrenna, and P. Z. Skands, "A Brief Introduction to PYTHIA 8.1", *Comput. Phys. Commun.* **178** (2008) 852–867, `doi:10.1016/j.cpc.2008.01.036`, `arXiv:0710.3820`.

[39] J. Alwall et al., "The automated computation of tree-level and next-to-leading order differential cross sections, and their matching to parton shower simulations", *JHEP* **07** (2014) 079, `doi:10.1007/JHEP07(2014)079`, `arXiv:1405.0301`.

[40] S. Alioli, P. Nason, C. Oleari, and E. Re, "NLO single-top production matched with shower in POWHEG: s- and t-channel contributions", *JHEP* **09** (2009) 111, `doi:10.1007/JHEP02(2010)011,10.1088/1126-6708/2009/09/111`, `arXiv:0907.4076`. [Erratum: JHEP02,011(2010)].

[41] CMS Collaboration, "Measurement of differential top-quark pair production cross sections in the lepton+jets channel in pp collisions at 8 TeV", Technical Report CMS-PAS-TOP-12-027, CERN, Geneva, 2013.

[42] CMS Collaboration, "Measurement of the differential cross section for top quark pair production in pp collisions at $\sqrt{s} = 8\,\mathrm{TeV}$", *Eur. Phys. J. C.* **75** (2015), no. 11, 542, `doi:10.1140/epjc/s10052-015-3709-x`, `arXiv:1505.04480`.

[43] CMS Collaboration, "Measurements of inclusive W and Z cross sections in pp collisions at $\sqrt{s} = 7$ TeV", *JHEP* **01** (2011) 080, `doi:10.1007/JHEP01(2011)080`, `arXiv:1012.2466`.

[44] CMS Collaboration, “CMS Luminosity Measurement for the 2015 Data Taking Period”, Technical Report CMS-PAS-LUM-15-001, CERN, Geneva, 2016.

[45] A. D. Martin, W. J. Stirling, R. S. Thorne, and G. Watt, “Parton distributions for the LHC”, *Eur. Phys. J. C.* **63** (2009) 189–285, `doi:10.1140/epjc/s10052-009-1072-5`, `arXiv:0901.0002`.

[46] A. D. Martin, W. J. Stirling, R. S. Thorne, and G. Watt, “Uncertainties on alpha(S) in global PDF analyses and implications for predicted hadronic cross sections”, *Eur. Phys. J. C.* **64** (2009) 653–680, `doi:10.1140/epjc/s10052-009-1164-2`, `arXiv:0905.3531`.

[47] The LHC Higgs Cross Section Working Group Collaboration, “Handbook of LHC Higgs Cross Sections: 4. Deciphering the Nature of the Higgs Sector”, `arXiv:1610.07922`.

[48] L. Moneta et al., “The RooStats Project”, *PoS* **ACAT2010** (2010) 057, `arXiv:1009.1003`.

[49] LHC Higgs Cross Section Working Group Collaboration, “Handbook of LHC Higgs Cross Sections: 3. Higgs Properties”, `doi:10.5170/CERN-2013-004`, `arXiv:1307.1347`.

[50] R. V. Harlander, S. Liebler, and H. Mantler, “SusHi: A program for the calculation of Higgs production in gluon fusion and bottom-quark annihilation in the Standard Model and the MSSM”, *Comput. Phys. Commun.* **184** (2013) 1605–1617, `doi:10.1016/j.cpc.2013.02.006`, `arXiv:1212.3249`.

[51] M. Spira, A. Djouadi, D. Graudenz, and P. M. Zerwas, “Higgs boson production at the LHC”, *Nucl. Phys. B.* **453** (1995) 17–82, `doi:10.1016/0550-3213(95)00379-7`, `arXiv:hep-ph/9504378`.

[52] R. V. Harlander and M. Steinhauser, “Supersymmetric Higgs production in gluon fusion at next-to-leading order”, *JHEP* **09** (2004) 066, `doi:10.1088/1126-6708/2004/09/066`, `arXiv:hep-ph/0409010`.

[53] R. Harlander and P. Kant, “Higgs production and decay: Analytic results at next-to-leading order QCD”, *JHEP* **12** (2005) 015, `doi:10.1088/1126-6708/2005/12/015`, `arXiv:hep-ph/0509189`.

[54] G. Degrassi and P. Slavich, “NLO QCD bottom corrections to Higgs boson production in the MSSM”, *JHEP* **11** (2010) 044, `doi:10.1007/JHEP11(2010)044`, `arXiv:1007.3465`.

[55] G. Degrassi, S. Di Vita, and P. Slavich, “NLO QCD corrections to pseudoscalar Higgs production in the MSSM”, *JHEP* **08** (2011) 128, `doi:10.1007/JHEP08(2011)128`, `arXiv:1107.0914`.

[56] G. Degrassi, S. Di Vita, and P. Slavich, “On the NLO QCD Corrections to the Production of the Heaviest Neutral Higgs Scalar in the MSSM”, *Eur. Phys. J. C.* **72** (2012) 2032, `doi:10.1140/epjc/s10052-012-2032-z`, `arXiv:1204.1016`.

[57] R. V. Harlander and W. B. Kilgore, “Next-to-next-to-leading order Higgs production at hadron colliders”, *Phys. Rev. Lett.* **88** (2002) 201801, `doi:10.1103/PhysRevLett.88.201801`, `arXiv:hep-ph/0201206`.

[58] C. Anastasiou and K. Melnikov, "Higgs boson production at hadron colliders in NNLO QCD", *Nucl. Phys. B.* **646** (2002) 220–256, `doi:10.1016/S0550-3213(02)00837-4`, `arXiv:hep-ph/0207004`.

[59] V. Ravindran, J. Smith, and W. L. van Neerven, "NNLO corrections to the total cross-section for Higgs boson production in hadron hadron collisions", *Nucl. Phys. B.* **665** (2003) 325–366, `doi:10.1016/S0550-3213(03)00457-7`, `arXiv:hep-ph/0302135`.

[60] R. V. Harlander and W. B. Kilgore, "Production of a pseudoscalar Higgs boson at hadron colliders at next-to-next-to leading order", *JHEP* **10** (2002) 017, `doi:10.1088/1126-6708/2002/10/017`, `arXiv:hep-ph/0208096`.

[61] C. Anastasiou and K. Melnikov, "Pseudoscalar Higgs boson production at hadron colliders in NNLO QCD", *Phys. Rev. D.* **67** (2003) 037501, `doi:10.1103/PhysRevD.67.037501`, `arXiv:hep-ph/0208115`.

[62] U. Aglietti, R. Bonciani, G. Degrassi, and A. Vicini, "Two loop light fermion contribution to Higgs production and decays", *Phys. Lett. B.* **595** (2004) 432–441, `doi:10.1016/j.physletb.2004.06.063`, `arXiv:hep-ph/0404071`.

[63] R. Bonciani, G. Degrassi, and A. Vicini, "On the Generalized Harmonic Polylogarithms of One Complex Variable", *Comput. Phys. Commun.* **182** (2011) 1253–1264, `doi:10.1016/j.cpc.2011.02.011`, `arXiv:1007.1891`.

[64] S. Dittmaier, M. Kramer, 1, and M. Spira, "Higgs radiation off bottom quarks at the Tevatron and the CERN LHC", *Phys. Rev. D* **70** (2004) 074010, `doi:10.1103/PhysRevD.70.074010`, `arXiv:hep-ph/0309204`.

[65] S. Dawson, C. B. Jackson, L. Reina, and D. Wackeroth, "Exclusive Higgs boson production with bottom quarks at hadron colliders", *Phys. Rev. D* **69** (Apr, 2004) 074027, `doi:10.1103/PhysRevD.69.074027`.

[66] R. V. Harlander and W. B. Kilgore, "Higgs boson production in bottom quark fusion at next-to-next-to-leading order", *Phys. Rev. D* **68** (Jul, 2003) 013001, `doi:10.1103/PhysRevD.68.013001`.

[67] R. Harlander, M. Kramer, and M. Schumacher, "Bottom-quark associated Higgs-boson production: reconciling the four- and five-flavour scheme approach", `arXiv:1112.3478`.

[68] S. Heinemeyer, W. Hollik, and G. Weiglein, "FeynHiggs: A Program for the calculation of the masses of the neutral CP even Higgs bosons in the MSSM", *Comput. Phys. Commun.* **124** (2000) 76–89, `doi:10.1016/S0010-4655(99)00364-1`, `arXiv:hep-ph/9812320`.

[69] S. Heinemeyer, W. Hollik, and G. Weiglein, "The Masses of the neutral CP - even Higgs bosons in the MSSM: Accurate analysis at the two loop level", *Eur. Phys. J. C.* **9** (1999) 343–366, `doi:10.1007/s100529900006`, `10.1007/s100520050537`, `arXiv:hep-ph/9812472`.

[70] G. Degrassi et al., "Towards high precision predictions for the MSSM Higgs sector", *Eur. Phys. J. C.* **28** (2003) 133–143, `doi:10.1140/epjc/s2003-01152-2`, `arXiv:hep-ph/0212020`.

[71] M. Frank et al., "The Higgs Boson Masses and Mixings of the Complex MSSM in the Feynman-Diagrammatic Approach", *JHEP* **02** (2007) 047, `doi:10.1088/1126-6708/2007/02/047`, `arXiv:hep-ph/0611326`.

[72] T. Hahn et al., "High-Precision Predictions for the Light CP -Even Higgs Boson Mass of the Minimal Supersymmetric Standard Model", *Phys. Rev. Lett.* **112** (2014), no. 14, 141801, `doi:10.1103/PhysRevLett.112.141801`, `arXiv:1312.4937`.

[73] A. Djouadi, J. Kalinowski, and M. Spira, "HDECAY: A Program for Higgs boson decays in the standard model and its supersymmetric extension", *Comput. Phys. Commun.* **108** (1998) 56–74, `doi:10.1016/S0010-4655(97)00123-9`, `arXiv:hep-ph/9704448`.